Synthesis of Iron Sulfide Nanocrystals Encapsulated in Highly Porous Carbon-Coated CNT Microsphere as Anode Materials for Sodium-Ion Batteries

Yeong Beom Kim, Hyo Yeong Seo, Kyeong-Ho Kim, Jung Sang Cho, Yun Chan Kang,* and Gi Dae Park**

Highly porous carbon materials with a rationally designed pore structure can be utilized as reservoirs for metal or nonmetal components. The use of small-sized metal or metal compound nanoparticles, completely encapsulated by carbon materials, has attracted significant attention as an effective approach to enhancing sodium ion storage properties. These materials have the ability to mitigate structural collapse caused by volume expansion during the charging process, enable short ion transport length, and prevent polysulfide elution. In this study, a concept of highly porous carbon-coated carbon nanotube (CNT) porous microspheres, which serve as excellent reservoir materials is suggested and a porous microsphere is developed by encapsulating iron sulfide nanocrystals within the highly porous carbon-coated CNTs using a sulfidation process. Furthermore, various sulfidation processes to determine the optimal method for achieving complete encapsulation are investigated by comparing the morphologies of diverse iron sulfide-carbon composites. The fully encapsulated structure, combined with the porous carbon, provides ample space to accommodate the significant volume changes during cycling. As a result, the porous iron sulfide-carbon-CNT composite microspheres exhibited outstanding cycling stability (293 mA h g^{-1} over 600 cycles at 1 A g^{-1}) and remarkable rate capability (100 mA h g^{-1} at 5 A g^{-1}).

1. Introduction

Highly porous carbon materials with a nanostructured pore architecture have been utilized as reservoirs for metal or nonmetal components.[1–5] The developed micro- and mesoporous voids in carbon materials can incorporate small metal or metal compound nanocrystals through an infiltration process at liquified states. By embedding the metal or metal compound nanocrystals in small pores and subjecting them to a sintering heat treatment, the crystal growth can be effectively suppressed due to the favorable growth conditions. The utilization of small-sized metal or metal compound nanoparticles has garnered significant attention in various fields such as energy storage, catalysis, separation, and optoelectronics.[6–9] Moreover, the infiltration of small-sized nonmetals into porous carbon materials has also gained considerable interest, thanks to their enhanced reactivity and inhibition of elution, for example, lithium polychalcogenides (sulfide or selenide).[10–12]

Nanostructured carbon materials containing ultrafine metal, metal compounds, or nonmetal components have the potential to greatly influence the electrical conductivity and structural flexibility of electrode materials used in rechargeable batteries. Among these materials, porous nanostructures are particularly noteworthy for energy storage applications due to their ability to mitigate structural collapse caused by volume expansion during the charging process, their short ion transport length, and their rapid electrolyte penetration.[13–18] The shape of the carbon materials, along with the incorporation of enhanced conductive carbon composites,

---

Y. B. Kim, H. Y. Seo, G. D. Park
Department of Advanced Materials Engineering
Chungbuk National University
Chungdae-ro 1, Seowon-gu, Cheongju 28644, Republic of Korea
E-mail: gdpark@chungbuk.ac.kr

Y. B. Kim, Y. C. Kang
Department of Materials Science and Engineering
Korea University
Anam-dong, Seongbuk-gu, Seoul 136–713, Republic of Korea
E-mail: yckang@korea.ac.kr

K.-H. Kim
Department of Mechanical Engineering
Massachusetts Institute of Technology
Cambridge, MA 02139, USA

K.-H. Kim
Department of Materials Science and Engineering
Pukyong National University
45, Yongso-ro, Nam-Gu, Busan 48513, Republic of Korea

J. S. Cho
Department of Engineering Chemistry
Chungbuk National University
Chungdae-ro 1, Seowon-gu, Cheongju 28644, Republic of Korea
E-mail: jscho@cbnu.ac.kr

The ORCID identification number(s) for the author(s) of this article can be found under https://doi.org/10.1002/smll.202305686

DOI: 10.1002/smll.202305686

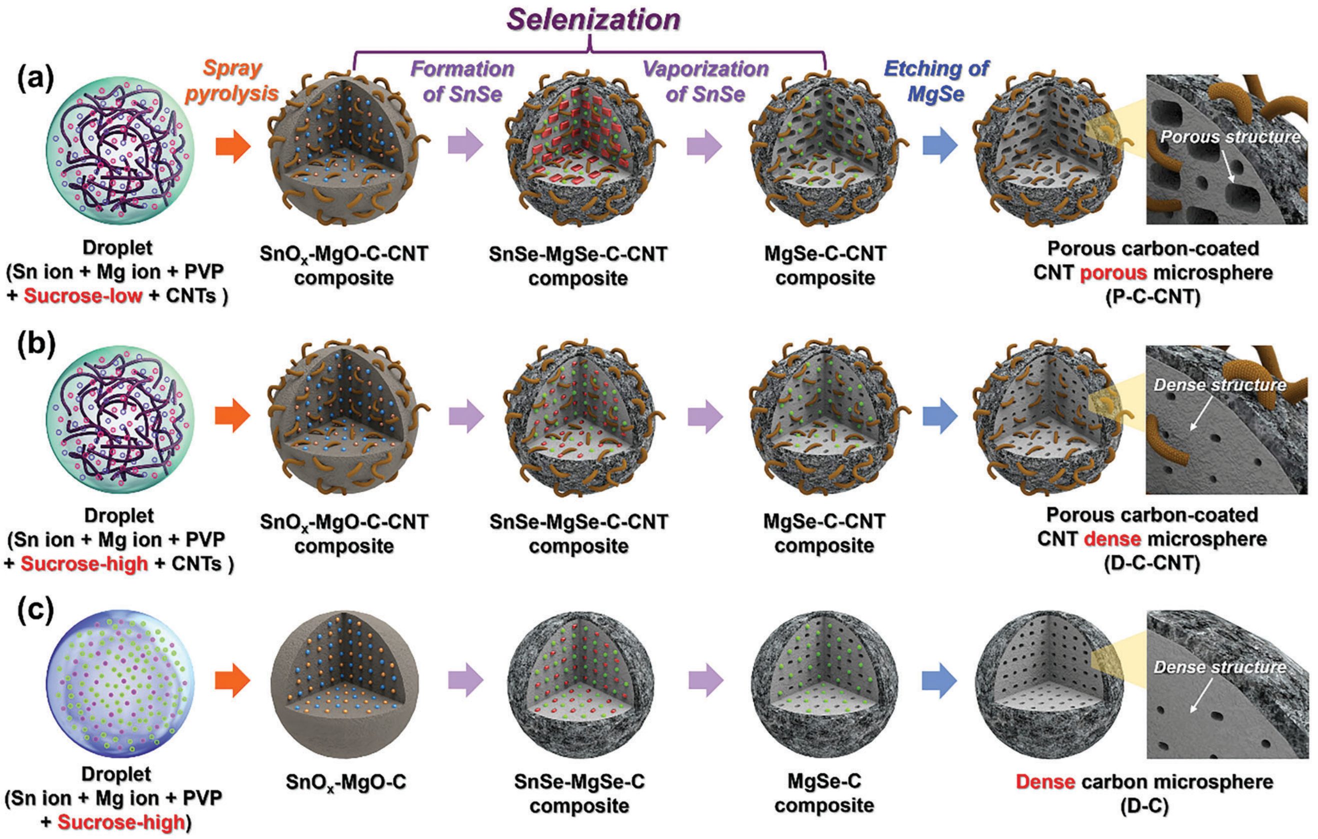

Scheme 1. Schematic illustration of formation mechanisms for a) porous carbon-coated CNT porous microsphere, b) porous carbon-coated CNT dense microsphere, and c) dense carbon microsphere with different sucrose content and presence or absence of CNT component. The sucrose contents were calculated from PVP/sucrose weight ratio, where the ratio of 1/2 corresponds to sucrose-low and the ratio of 1/8 corresponds to sucrose-high, respectively.

plays a vital role in developing electrode materials with improved electrochemical properties. One notable example is the utilization of one-dimensional (1D) carbon nanotubes (CNTs) as conductive agents in combination with various transition metal compounds. Additionally, three-dimensional (3D) CNT architectures composed of interconnected 1D CNTs with incorporated metal compounds have been extensively studied as efficient anode materials for alkali-ion batteries.[19,20]

Compared to lithium-ion batteries, the electrochemical characteristics of sodium-ion batteries, such as specific capacity, cycling lifespan, and rate capability, are primarily determined by the small size and encapsulated position of the active materials.[21–23] Due to the significant volume change and slow ion mobility during sodiation and desodiation processes, the use of ultrafine metal compound nanocrystals, completely encapsulated by carbon components, has been proposed as an effective strategy for enhancing the sodium ion storage properties.[24–26] In this regard, nanostructured carbon materials containing ultrafine metal compound nanocrystals emerge as promising candidates capable of delivering superior electrochemical performance as anode materials for sodium-ion batteries.

In this study, we propose a concept of highly porous carbon-coated CNT porous microspheres, which serve as excellent reservoir materials. The precursor microspheres, containing tin, magnesium, PVP, and sucrose-derived carbon, were initially prepared through spray pyrolysis. These precursor microspheres were then transformed into highly porous carbon-coated CNT porous microspheres by eliminating the tin and magnesium components using selenium gas. The core and shell of the microspheres were coated with PVP and sucrose, respectively, creating impregnation spaces for metal and nonmetal salts. Additionally, the porosity of the yolk part was controlled by adjusting the amount of sucrose, enabling the formation of either porous or dense microstructures. Subsequently, a porous microsphere was developed by encapsulating iron sulfide nanocrystals within the highly porous carbon-coated CNTs using a sulfidation process. Special attention was given to exploring suitable sulfidation methods to achieve complete encapsulation of the iron sulfide nanocrystals. The resulting electrode materials were then evaluated for their potential as anode materials in sodium-ion batteries.

2. Results and Discussion

The formation mechanism of the highly porous carbon-coated CNT porous microspheres is visually depicted in **Scheme 1**. The spray pyrolysis process serves as the basis for the starting precursor material. In Scheme 1a, the droplet containing tin, magnesium salt, acid-treated CNTs, sucrose, and polyvinylpyrrolidone (PVP) undergoes drying and decomposition during spray

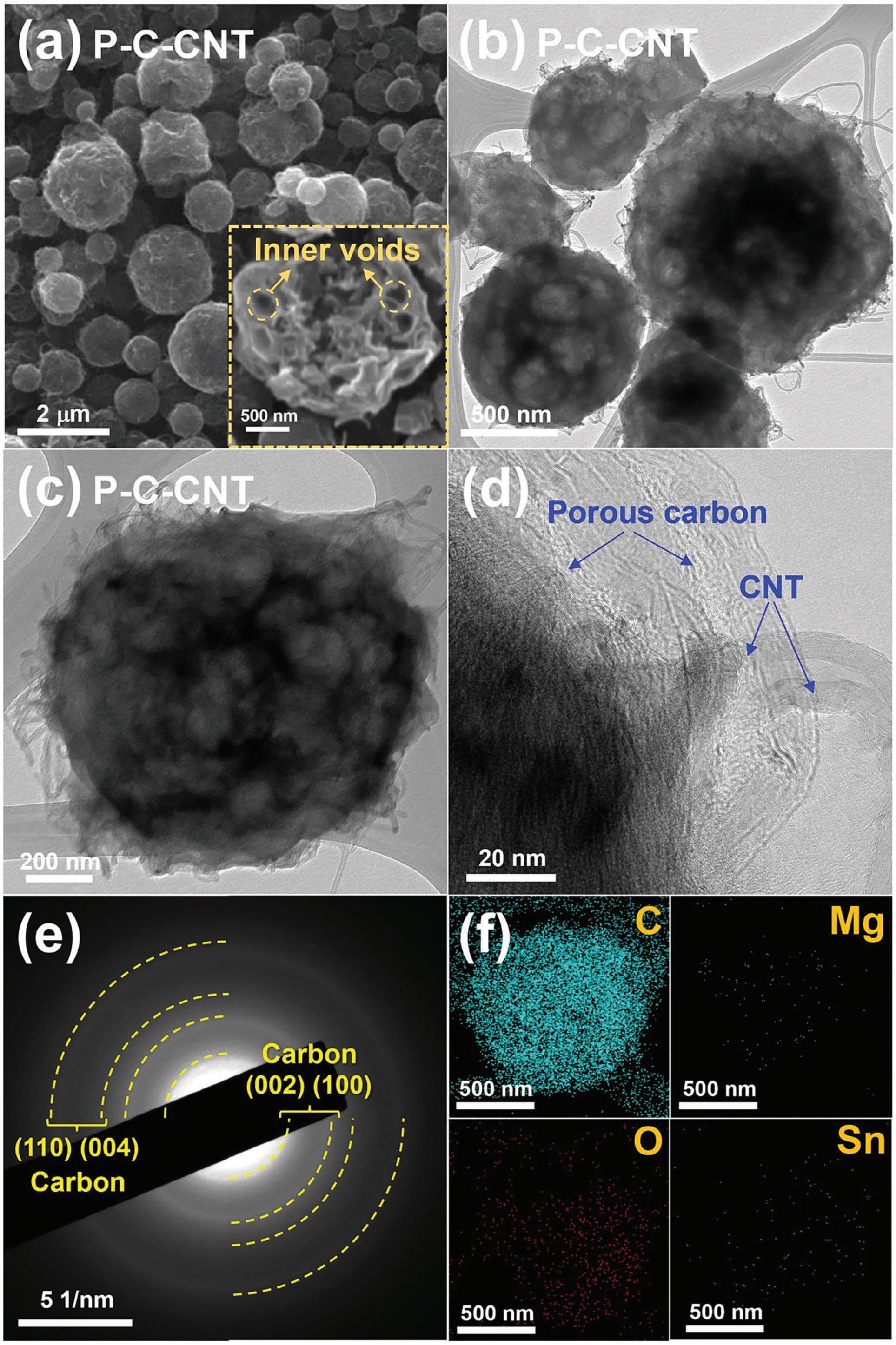

Figure 1. Morphological characteristics of P-C-CNT microspheres: a) SEM image, b,c) TEM images, d) HR-TEM image, e) SAED pattern, and f) elemental mapping images.

pyrolysis, resulting in the formation of SnO_x-MgO-C-CNT composite microspheres. Each component (SnO_x, MgO nanocrystals, and CNTs) is uniformly compounded on a nanoscale inside the microspheres. However, PVP and sucrose, as carbon sources, exhibit partial phase segregation during the spray pyrolysis, as reported in previous literature.[10,21] The prepared precursor (SnO_x-MgO-C-CNT composite) is then transformed into a porous carbon-coated CNT microsphere containing magnesium selenide nanocrystals through the elimination of tin components during the selenization process. Finally, the porous

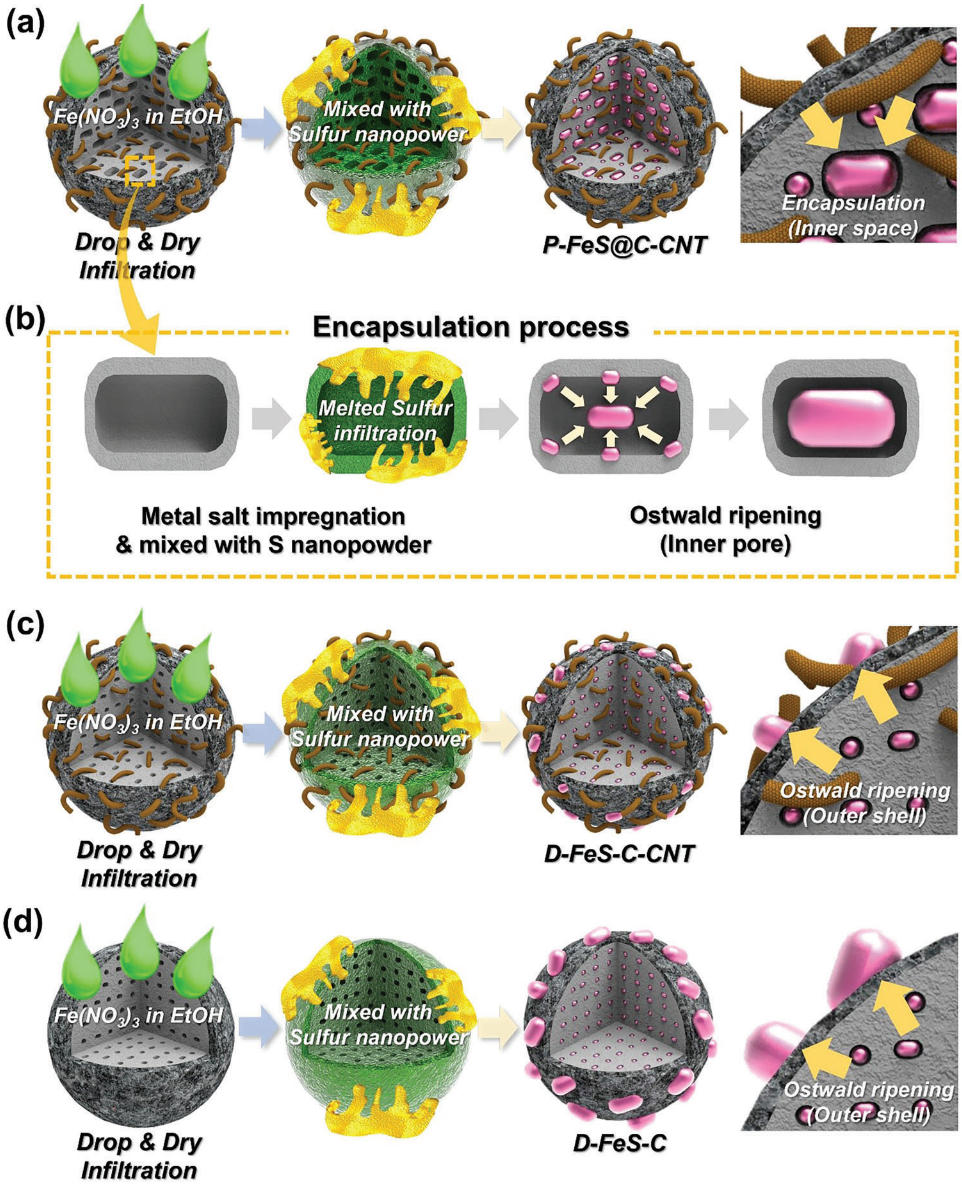

Scheme 2. Schematic illustration of sulfidation processes of iron nitrate infiltrated P-C-CNT, D-C-CNT, and D-C: a) sulfidation process for the fabrication of small-sized iron sulfide nanocrystals encapsulated in P-C-CNT, b) formation mechanism of completely encapsulated iron sulfide nanocrystals in the inner voids of P-C-CNT. Sulfidation processes for the fabrication of larger-sized iron sulfide nanocrystals located on the outer surface of c) D-C-CNT and d) D-C.

carbon-coated CNT porous microspheres (denoted as P-C-CNT) are obtained by removing the magnesium selenide nanocrystals through an acid-based etching process. The amount of sucrose in the spray solution determined the porous or dense shape of the carbon microsphere. In specific, the presence of low sucrose concentration (denoted as sucrose-low in Scheme 1a) led to significant crystal growth of tin selenide due to a small amount of sucrose-derived carbon, resulting in the formation of porous internal voids via the evaporation process of tin selenide. In Scheme 1b,c, increased amounts of sucrose (denoted as sucrose-high in Scheme 1b) in the spray solution are applied, leading to the formation of a densely structured core part. During the selenization process, the carbon derived from sucrose surrounds the tin selenide and magnesium selenide nanocrystals and fills the core part. By etching the metal selenide nanocrystals, porous carbon-coated CNT dense microspheres (denoted as D-C-CNT) and dense carbon microspheres (denoted as D-C) are produced as comparative samples, respectively.

The morphological characteristics of the sprayed precursor powders are presented in Figure S1, Supporting Information, showcasing the differences based on the presence or absence of CNT and the amount of sucrose. In all the precursor particles, highly uniform composites of SnO$_x$, MgO nanocrystals, and carbon sources are observed on a nanoscale within the microspheres. However, during the spray pyrolysis, phase separation occurs between PVP and sucrose-derived carbons. PVP migrates towards the outer shell, while sucrose assembles in the inner core, resulting in the formation of core-shell structured microspheres. Figure S1a,b, Supporting Information, clearly depicts the core-shell structure of SnO_x-MgO-C-CNT when an appropriate amount of sucrose is applied, which is further supported by TEM images in Figure S2, Supporting Information. However, as the amount of sucrose increases, leading to core filling, a dense structured core shape is observed in Figure S1c,d, Supporting Information. In the absence of CNT in the spray solution, microspheres with smooth surfaces are observed as shown in Figure S1e,f, Supporting Information. All three precursor powders exhibit low crystallinity due to the short-time pyrolysis during the spray process, as shown in XRD data (Figure S3, Supporting Information).

The morphological properties of pure carbon microspheres, including P-C-CNT, D-C-CNT, and D-C with different inner spaces and types, were obtained by removing tin selenide and magnesium selenide nanocrystals from the spray precursor. The morphological characteristics of these microspheres are shown in **Figure 1** and Figure S4, Supporting Information. Low-magnification SEM images of the three samples (Figure 1a, and Figures S4a and S4c, Supporting Information) reveal spherical morphologies, and the slightly irregular particle size distribution is attributed to the formation of one microsphere from one droplet, which varies in size due to the spray generator. P-C-CNT microspheres exhibit short CNT threads on their surfaces, while the other samples have smooth surfaces. SEM images of broken carbon microspheres (Figure 1a, and Figures S4b and S4d, Supporting Information) provide insights into their spatial structures. TEM images (Figure 1b,c) indicate that P-C-CNT microspheres possess a porous internal structure with multiple voids. The mean size of the pores was calculated as about 140 nm (Figure 1c). The highly porous carbon material is uniformly coated on the CNTs, providing ample space for infiltrating solutions containing metal and nonmetal salts, as indicated by the arrows in Figure 1d. The shell of the microsphere primarily consists of carbon derived from PVP due to the phase segregation during the spray pyrolysis, as shown in Figure 1d. Selected area electron diffraction (SAED) patterns and elemental mapping images (Figure 1e,f) confirm the presence of pure carbon and complete elimination of Sn and Mg components. The complete removal of Sn and Mg components was further confirmed by EDS data in Figure S5 and Table S1, Supporting Information. Conversely, SEM images of broken D-C-CNT and D-C microspheres (Figures S4b and S4d, Supporting Information) reveal a densely structured core part resulting from increased amounts of sucrose. XRD patterns of the three carbon microspheres confirm the formation of pure carbon components after the complete etching process of tin and magnesium selenides, as shown in Figure S6, Supporting Information. The Brunauer–Emmett–Teller (BET) surface areas and pore structures of the carbon microspheres were analyzed through N_2 gas adsorption and desorption isotherms, as well as Barrett–Joyner–Halenda (BJH) measurement (Figure S7, Supporting Information). The BET surface areas of P-C-CNT, D-C-CNT, and D-C were 1452, 1022, and 1019 $m^2\ g^{-1}$, respectively, with corresponding pore volumes of 0.90, 0.58, and 0.55 $cm^3\ g^{-1}$. The removal of metal selenide nanocrystals and carbonization of carbon sources (sucrose and PVP) contribute to the high specific surface area of the carbon microspheres.[21] Among them, P-C-CNT exhibits the highest surface area and pore volume due to its porous structure and etching of small-sized metal compounds. It is worth noting that the pore volume of micro- and mesopores decreases as the sucrose content increases. Additionally, the developed pore diameter of ≈4.3 nm in P-C-CNT and D-C-CNT is not observed in D-C, indicating a greater development of mesopores due to the complexation with CNTs.

The newly developed carbon microspheres (P-C-CNT, D-C-CNT, and D-C) can be utilized as reservoir materials for metal or nonmetal components. **Scheme 2** provides a schematic illustration of the strategies employed to synthesize the porous microsphere with iron sulfide nanocrystals encapsulated in a highly porous carbon-coated CNT. In Scheme 2a, the prepared porous carbon-coated CNT porous microsphere (P-C-CNT) was impregnated with an infiltration solution containing iron nitrate. This solution deeply infiltrated the porous carbon surrounding the CNTs due to capillary forces, as shown in Scheme 2a. The infiltrated powder (iron nitrate-P-C-CNT composite) was then uniformly mixed with sulfur nanopowders. Subsequently, the mixed sulfur powders were melted and infiltrated into a porous carbon channel during heat treatment, resulting in the formation and growth of iron sulfide nanocrystals within the developed porous voids through the Ostwald ripening effect as depicted in Scheme 2b. This process led to the formation of a porous microsphere with iron sulfide nanocrystals encapsulated in a highly porous carbon-coated CNT (denoted as P-FeS@C-CNT). In contrast, when the same conditions for iron sulfide formation were applied to D-C-CNT and D-C the immediately formed iron sulfide nanocrystals were pushed outward and grew since the iron sulfide nanocrystals had no internal voids, as shown in Scheme 2c,d. Consequently, comparative samples were formed with iron sulfide nanocrystals decorating highly porous carbon in two variations: one with CNT (referred to as D-FeS-C-CNT) and the other without (referred to as D-FeS-C). Notably, in the absence of CNT, the iron sulfide nanocrystals are prone to more significant Ostwald ripening, resulting in larger crystal sizes, as shown in Scheme 2d.

The morphological characteristics of P-FeS@C-CNT are illustrated in **Figure 2**. The SEM and TEM images in Figures 2a and 2b demonstrated that the spherical microsphere composed of iron sulfide nanocrystals, carbon, and CNTs exhibited non-aggregated properties. Notably, it was evident that the iron sulfide nanocrystals were almost completely absent on the surface of the microsphere, indicating their encapsulation within the porous carbon-coated CNT. The carbon shell, derived from PVP through phase segregation of PVP and sucrose, was clearly observed as indicated by the arrow in Figure 2c. The outer carbon shell, in addition to the space inside the microsphere, played a crucial role in preventing the escape of iron sulfide nanocrystals to the external environment. Within the porous inner voids, the iron sulfide nanocrystals were situated as shown in Figure 2d. The high-resolution TEM image in Figure 2d revealed distinct lattice fringes with separations of 0.30 and 0.27 nm, corresponding to the (110) and (112) crystal planes of $Fe_{0.975}S$ and FeS phases, respectively. The SAED pattern in Figure 2e confirmed the presence of $Fe_{0.975}S$ and FeS phases in P-FeS@C-CNT. The elemental mapping images in Figure 2f demonstrated that the iron sulfide nanocrystals were uniformly embedded within the porous carbon matrix. The

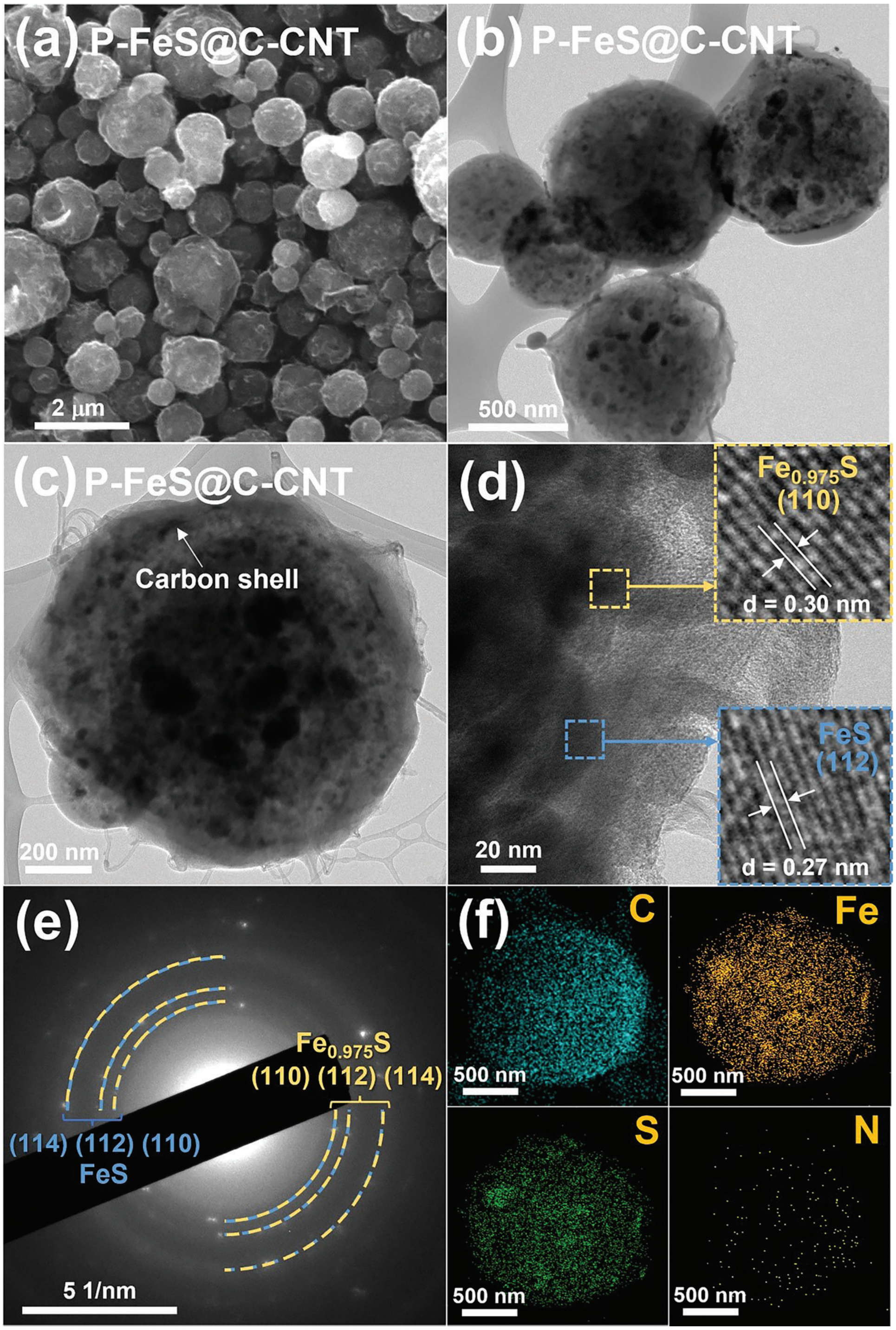

Figure 2. Morphological characteristics of P-FeS@C-CNT microspheres: a) SEM image, b,c) TEM images, d) HR-TEM image, e) SAED pattern, and f) elemental mapping images.

presence of nitrogen, derived from the decomposition of PVP, further supported the formation of the N-doped carbon shell.

The morphologies of D-FeS-C-CNT and D-FeS-C in **Figure 3** exhibited clear differences compared to those of P-FeS@C-CNT. In the SEM and TEM images of D-FeS-C-CNT shown in Figure 3a,b, a grainy surface was observed on the microspheres, as indicated by arrows. This grainy surface consisted of iron sulfide nanocrystals that were formed by being pushed outward due to the absence of voids inside the microsphere, as a result of Ostwald ripening. Figure 3c,d simultaneously displayed small-sized nanocrystals embedded in the dense carbon microsphere and relatively larger-sized nanocrystals exposed on the surface. The

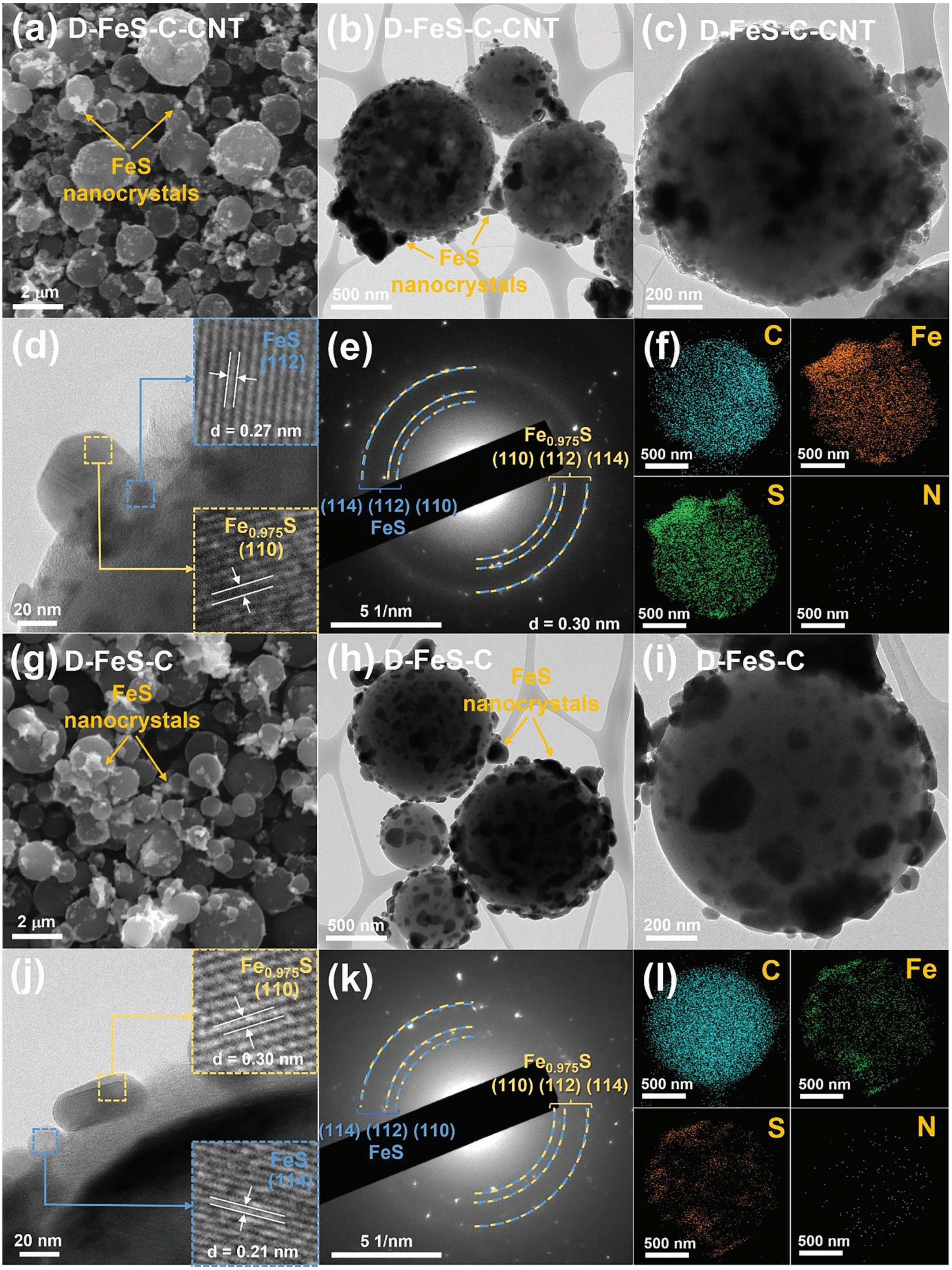

Figure 3. Morphological characteristics of a–f) D-FeS-C-CNT and g–l) D-FeS-C microspheres: a,g) SEM images, b,c,h,i) TEM images, d,j) HR-TEM images, e,k) SAED patterns, and f,l) elemental mapping images.

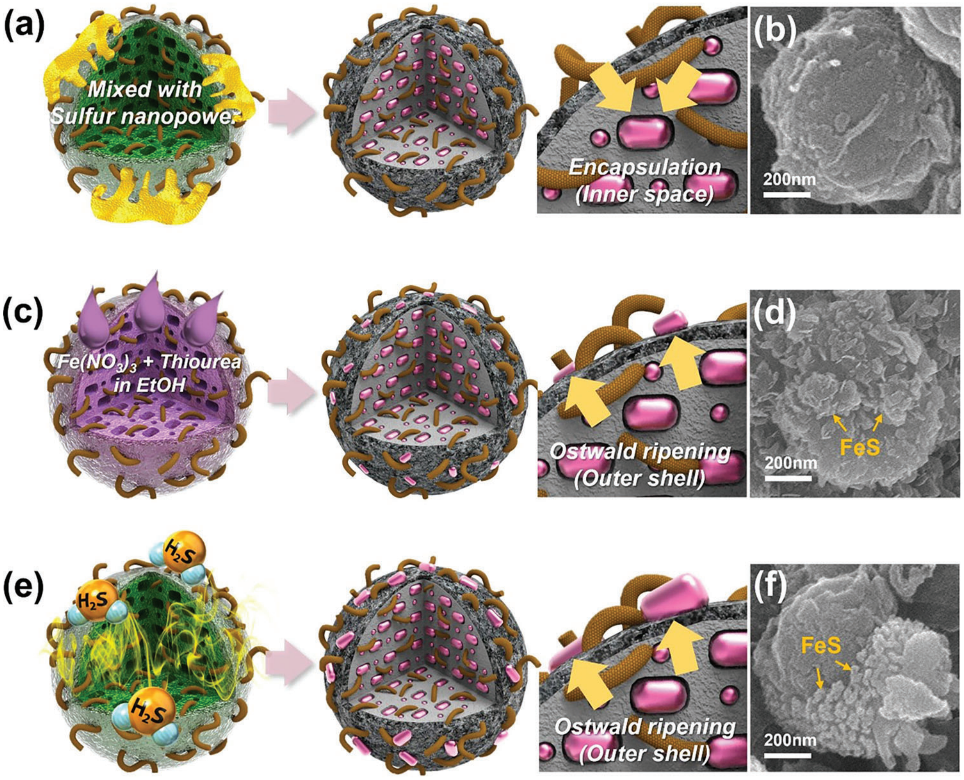

Figure 4. Schematic illustration of various sulfidation methods and SEM images of FeS-C-CNT composite microspheres fabricated by following processes: a) sulfidation of iron-nitrate infiltrated powders mixed with sulfur nanopowders, b) SEM image, c) sulfidation of powders infiltrated with mixture of iron-nitrate and thiourea, d) SEM image, e) sulfidation of iron-nitrate infiltrated powders under H_2S gas atmosphere, and f) SEM image.

HR-TEM image in Figure 3d revealed distinct lattice fringes separated by 0.30 and 0.27 nm, corresponding to the (110) and (112) crystal planes of $Fe_{0.975}S$ and FeS phases, respectively. Additionally, the SAED pattern in Figure 3e confirmed the presence of $Fe_{0.975}S$ and FeS phases, indicating that both P-FeS@C-CNT and D-FeS-C-CNT shared the same crystal structure phase. The elemental mapping images also illustrated the presence of small-sized nanocrystals embedded in the dense carbon microsphere and relatively larger-sized nanocrystals exposed on the surface of D-FeS-C-CNT. The morphological characteristics of D-FeS-C (without the CNT component) were also shown in Figure 3g–l. Similar to D-FeS-C-CNT, a number of iron sulfide nanocrystals exposed on the surface were observed, as indicated by arrows in Figure 3g,h. Notably, the size of the exposed nanocrystals was relatively larger than that of D-FeS-C-CNT, as depicted in Figure 3i. Interestingly, the PVP-derived carbon shell and sucrose-derived carbon core were clearly distinguishable, as displayed in Figure 3j. Furthermore, in comparison to the D-FeS-C-CNT, a few iron sulfide nanocrystals embedded inside the carbon microsphere were observed in Figure 3j, suggesting that the presence of CNTs prevented the escape of iron sulfide through Ostwald ripening, as mentioned in Scheme 2d. The HR-TEM and SAED pattern in Figure 3j,k, respectively, exhibited values identical to those of D-FeS-C-CNT. The elemental mapping images in Figure 3l clearly demonstrated that the majority of iron sulfide nanocrystals were located on the outer surface of the microsphere.

In this study, the effect of encapsulating iron sulfide nanocrystals through the sulfidation method was investigated as described in **Figure 4**. Three different strategies were employed to convert iron nitrate into iron sulfide. The first method involved metal salt infiltration, where a solution containing iron nitrate was impregnated into the P-C-CNT reservoir. The infiltrated powders were then mixed with sulfur powders and reacted at high temperatures to form iron sulfide (as depicted in Figure 4a). The iron nitrate solution was able to penetrate the small inner pores of P-C-CNT through capillary action, thanks to its rich pore volume. Upon reaction with uniformly mixed sulfur, the initially melted sulfur penetrated additional pores in P-C-CNT, leading to the formation of iron sulfide nanocrystals within the inner pores. As a result, the iron nitrate-infiltrated P-C-CNT was successfully transformed into a porous microsphere with encapsulated iron sulfide nanocrystals, as illustrated in Scheme 2. SEM images in Figure 4b and Figure S8a, Supporting Information confirmed the absence of exposed nanocrystals on the microsphere surface, supporting the successful encapsulation. The second method (Figure 4c) involved metal and nonmetal co-infiltration, where a solution containing iron nitrate and thiourea (a sulfur source) was impregnated into the P-C-CNT reservoir. However, as shown in Figure 4d and Figure S8b, Supporting Information, crystal growth emerged from the microsphere surface, indicating that the iron sulfide crystals could not be sufficiently encapsulated within P-C-CNT. It can be inferred that during heat treatment when the impregnating solution was thoroughly

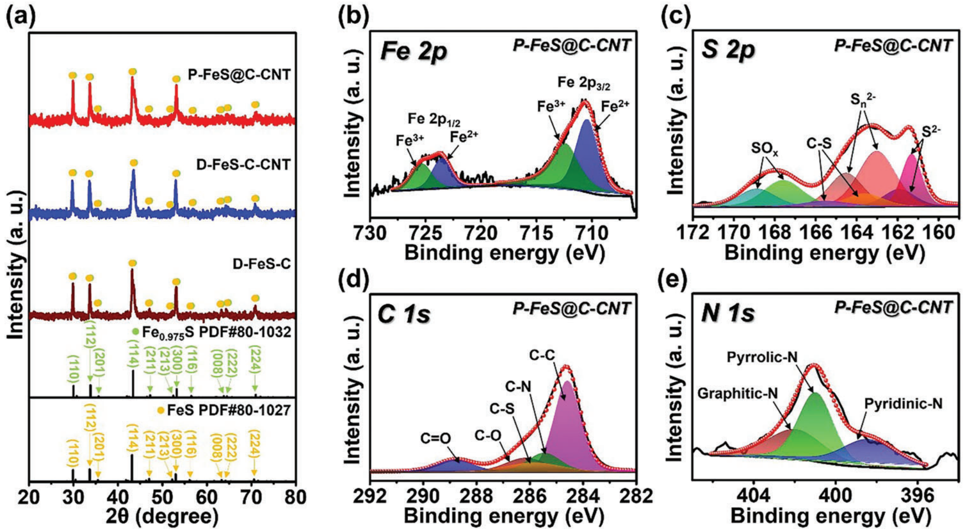

Figure 5. XRD patterns of three iron sulfide-carbon composites and XPS spectra of P-FeS@C-CNT: a) XRD patterns, b) Fe 2p spectrum, c) S 2p spectrum, d) C 1s spectrum, and e) N 1s spectrum.

absorbed into P-C-CNT, the melting of thiourea coincided with the elution of iron nitrate particles. Consequently, the encapsulation process was compromised. Similar to the second method, the third method resulted in a morphology comparable to that of the second method. This third method involved impregnating P-C-CNT with iron nitrate and subsequently heat-treating it under an H_2S gas atmosphere as shown in Figure 4e. The crystallization of iron sulfides occurred mainly from the outer regions of the P-C-CNT microsphere due to the presence of H_2S gas. Consequently, the iron sulfide nanocrystals were expelled from the microsphere through Ostwald ripening, as demonstrated in Figure 4f and Figure S8c, Supporting Information.

The crystal structures of P-FeS@C-CNT, D-FeS-CNT, and D-FeS-C were examined using X-ray diffraction (XRD), as shown in **Figure 5**a. All three samples exhibited the same crystal structures, specifically Pyrrhotite $Fe_{0.975}S$ (PDF#80-1032) and Troilite FeS (PDF#80-1027) solid solution. To further investigate the chemical bonding states in P-FeS@C-CNT, X-ray photoelectron spectroscopy (XPS) analysis was performed, as depicted in Figure 5b–e. The high-resolution Fe 2p XPS spectra displayed two distinct peaks corresponding to Fe $2p_{3/2}$ and Fe $2p_{1/2}$. The peaks were fitted at 712.4 and 725.3 eV, indicating Fe^{2+} (related to $Fe_{1-x}S$) and 712.4 and 725.3 eV for Fe^{3+} (related to Fe-SO_x).[27,28] In Figure 5c, the high-resolution S 2p spectra exhibited four categories: S^{2-}, $S_n^{\ 2-}$, SO_x, and C–S. The presence of S^{2-} peaks indicated the presence of iron sulfides, while the $S_n^{\ 2-}$ peaks suggested the existence of iron polysulfide species.[29,30] The SO_x peak corresponded to the partial oxidation of FeS during sample preparation under an air atmosphere, aligning with the Fe^{3+} peaks observed in Figure 5b.[29,31] Additionally, the C–S bonding peaks (located at 165.5 and 163.6 eV) indicated the presence of iron sulfide and carbon composites in P-FeS@C-CNT.[32] The C 1s spectra of P-FeS@C-CNT in Figure 5d were fitted to five peaks at 284.6, 285.5, 285.8, 286.1, and 288.7 eV, corresponding to sp^2-bonded carbon (C–C), N-doped carbon (C–N), C-S bonded carbon (C–S), epoxy and alkoxy groups (C–O), and carbonyl and carboxylic (O–C=O) components, respectively.[33,34] The presence of N-doped carbon in PVP-derived carbon is a characteristic reported in previous literature.[21] The N 1s spectrum in Figure 5e, originating from N-doped carbon, was deconvoluted into three peaks at 398.3, 400.9, and 402.0 eV, representing pyridinic N, pyrrolic N, and graphitic N, respectively.[33] The Raman spectra of the three samples (Figure S9, Supporting Information) commonly exhibited two prominent peaks at 1342 and 1592 cm^{-1}, which were assigned to disordered carbon (D-band) and graphitic carbon (G-band), respectively.[35,36] This indicated the presence of crystalline nature in the PVP- and sucrose-derived carbon and CNTs in all three samples. Thermogravimetry (TG) data of the three samples (Figure S10, Supporting Information) revealed similar weight loss patterns due to the conversion of iron sulfide to iron oxide and the combustion of the carbon component. Initially, all three samples showed weight increase up to 400 °C, which was attributed to the formation of iron sulfate through partial oxidation.[27,37] P-FeS@C-CNT and D-FeS-C-CNT exhibited a two-step weight loss: the first step was associated with the decomposition of carbon derived from PVP and sucrose as well as the oxidation of iron sulfide and iron sulfate, while the second step corresponded to the decomposition of CNTs. The decomposition of CNTs occurred at higher temperatures than the carbons derived from PVP and sucrose. In the case of D-FeS-C without CNTs, a single-step weight reduction was observed. The calculated carbon content in the three samples was 56 wt%, assuming a 1:1 weight ratio for $Fe_{0.975}S$ and FeS.

The electrochemical reaction mechanism of the iron sulfide-carbon composite samples was investigated using cyclic voltammetry (CV) measurements. The CV measurements were conducted within a potential range of ≈0.001 to 3.0 V (vs Na^+/Na) at a scan rate of 0.1 mV s^{-1}, as depicted in **Figure 6**. The three samples (P-FeS@C-CNT, D-FeS-C-CNT, and D-FeS-C) exhibited similar cathodic and anodic peaks during repeated cycling. As shown in Figure 6a, the P-FeS@C-CNT electrode exhibited an irreversible reduction peak at around 1.4 V at the initial discharging process. Compared to the D-FeS-C electrode (Figure 6c), this peak could be attributed to the irreversible reaction between the

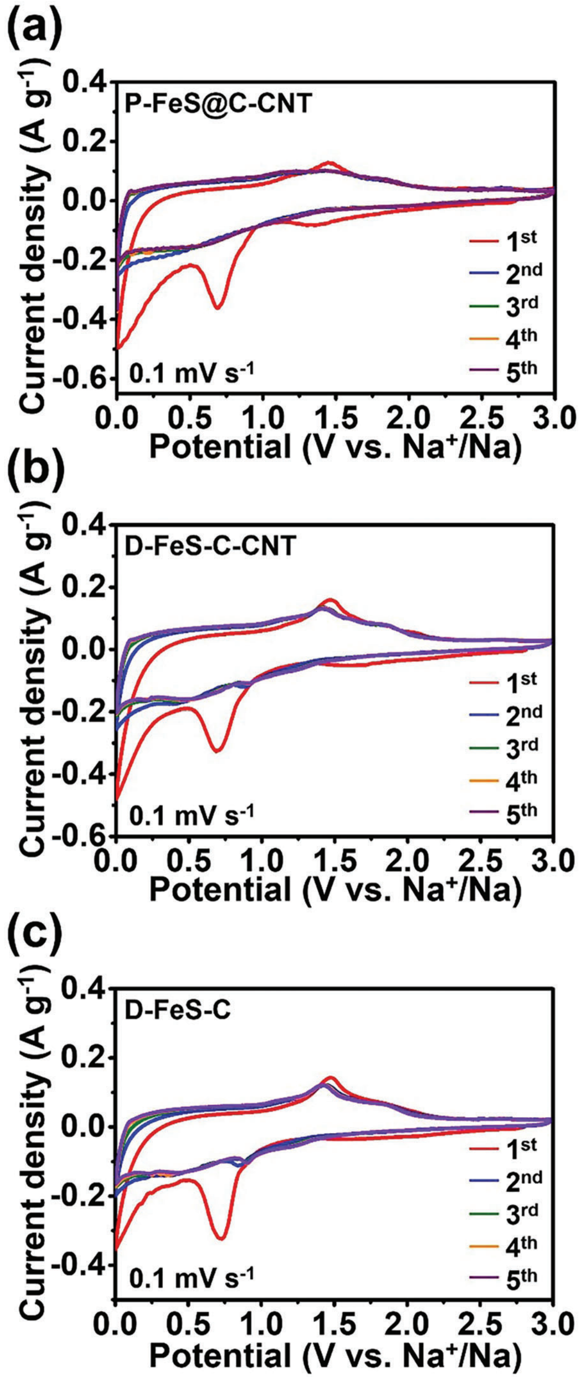

Figure 6. CV curves of a) P-FeS@C-CNT, b) D-FeS-C-CNT, and c) D-FeS-C at a scan rate of 0.1 mV s^{-1}.

sodium ion and the functional groups of the CNT component.[38] Moreover, all three electrodes showed broad and small peaks at ≈1.5 to 2.25 V during the initial discharging process. These broad peaks arise from the intercalation of sodium ions into iron sulfide nanocrystals at high voltage to form the Na_xFeS.[39] Importantly, despite the same contents of CNT components in both P-FeS@C-CNT and D-FeS-C-CNT, the D-FeS-C-CNT electrode (Figure 6b) exhibited an almost negligible peak, which was attributed to the CNT component (1.4 V). It could be due to the differences in the morphological characteristics of these electrodes. As shown in Figure 2c, the CNT component of the P-C-CNT microsphere was exposed on the surface due to the complete encapsulation of iron sulfide nanocrystals. Conversely, the CNT component of D-FeS-C-CNT (Figure 3c) was embedded in the dense carbon microsphere, and the large iron sulfide nanocrystals were exposed on the surface. Consequently, the irreversible reaction between the sodium ion and the functional groups of the CNT component within the D-FeS-C-CNT electrode was considerably limited. After these processes (≈1.5 to 2.25 and 1.4 V), two other prominent peaks were observed in all three electrodes. These peaks were related to the conversion from Na_xFeS to metallic Fe and Na_2S, as well as the generation of solid electrolyte interphase (SEI) layers (0.7 V), and the intercalation of sodium ions into the carbon components (0.01 V).[39,40] Therefore, the initial discharge reaction can be expressed as follows.

$$FeS + 2Na^+ + 2e^- \rightarrow Na_2S + Fe \tag{1}$$

During the subsequent charging process, two anodic peaks at 1.45 and 1.82 V were observed, attributed to the formation of Na_2FeS_2 and $Na_{2-x}FeS_2$, respectively.[39,40] All three samples demonstrated good reversibility during the initial five cycles. Based on this observation, the possible reaction mechanisms subsequent to the initial discharging are listed as follows.[39,40]

$$2Na_2S + Fe \leftrightarrow Na_2FeS_2 + 2Na^+ + 2e^- \tag{2}$$

$$Na_2FeS_2 \leftrightarrow Na_{2-X}FeS_2 + xNa^+ + xe^- \tag{3}$$

During the initial discharging and charging processes, the changes in resistance and sodium ion diffusion coefficients of the three samples (P-FeS@C-CNT, D-FeS-C-CNT, and D-FeS-C) were compared using in situ electrochemical impedance spectroscopy (EIS) measurements, as shown in **Figure 7**. The Nyquist plots, which were measured at specific potentials during the initial discharging and charging process, were collected and summarized in Figure 7a–c. These plots included contributions from the solution resistance (R_s), the interfacial layer associated with the SEI layer (R_{sei}), and the charge transfer resistance (R_{ct}). The variation of the total resistance ($R_{tot} = R_s + R_{sei} + R_{ct}$) during the initial cycle, obtained by in situ EIS at preselected potentials, was represented by corresponding colored dots in Figure 7d–f. All three samples exhibited a significant decrease in R_{tot} during the initial discharging process until ≈1.0 V. This decrease could be attributed to the initial sodiation process and the aging of the sodium ions, regardless of the sufficient aging time (6 h). Subsequently, phase transition, volume expansion due to the conversion reaction, and the formation of SEI layers (as confirmed by CV curves in Figure 6) led to an increase in electrode resistance.[41,42] Contrary to expectations, the R_{tot} values showed a slight decrease until the discharge was completed. This can be attributed to the transformation of large iron sulfide nanocrystals into ultrafine nanocrystals during the sodiation process, which had a larger effect on the total resistance of the electrode than the aforementioned reasons.[43,44] At the end of the initial discharge, the R_{tot} values for P-FeS@C-CNT, D-FeS-C-CNT, and D-FeS-C were 232, 369, and 271 Ω, respectively. The low resistance value

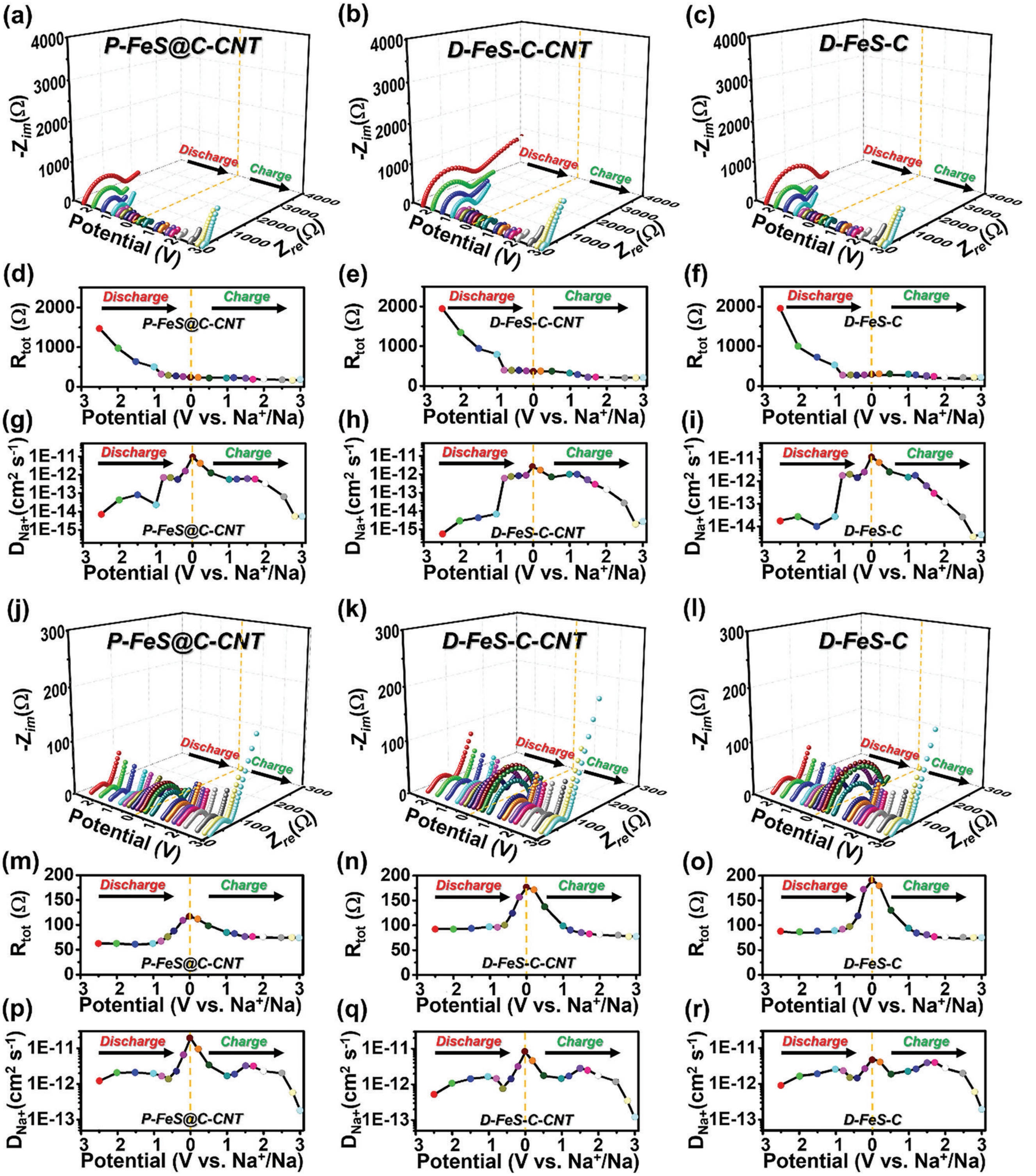

Figure 7. a–c) In situ EIS Nyquist plots of P-FeS@C-CNT, D-FeS-C-CNT, and D-FeS-C measured at preselected potentials during the first cycle, d–f) in situ EIS graphs (R_{tot} vs potential), and g-i) variations in sodium-ion diffusion coefficients calculated from in situ EIS results. j–l) In situ EIS Nyquist plots of P-FeS@C-CNT, D-FeS-C-CNT, and D-FeS-C measured at preselected potentials after 100 cycles, m–o) in situ EIS graphs (R_{tot} vs potential), and p–r) variations in sodium-ion diffusion coefficients calculated from in-situ EIS results.

of P-FeS@C-CNT can be attributed to its porous structure, small-sized iron sulfide nanocrystals, and the uniform composite with CNTs. Despite the presence of a conductive CNT component in D-FeS-C-CNT, its R_{tot} value is larger than that of D-FeS-C after the initial discharge. As observed from the morphological characteristics in Figure 3c,i, the iron sulfide nanocrystals in D-FeS-C-CNT were relatively located inside the core compared to D-FeS-C. P-FeS@C-CNT with a porous structure and D-FeS-C with exposed iron sulfide nanocrystals on the surface enables rapid electrolyte penetration and contact. This facilitates a fast conversion reaction from Na_xFeS to metallic Fe and Na_2S, as well as fast diffusion of sodium ions during the initial sodiation process. During the subsequent charging process, the R_{tot} of all three samples continuously decreased, possibly due to the volume contraction as well as the disappearance of the non-conductive Na_2S matrix.[45,46] As a result, the R_{tot} values for P-FeS@C-CNT, D-FeS-C-CNT, and D-FeS-C at the end of the initial charge were 172, 209, and 193 Ω, respectively. The sodium ion diffusion coefficient ($D_{\mathrm{Na+}}$) variations of the three samples, calculated using the following equation in the Nyquist plot, also showed good correlations with the R_{tot} variations in Figure 7d–f.

$$D_{\mathrm{Na}^+} = 0.5(RT/Sn^2F^2C\sigma)^2 \tag{4}$$

A detailed description of parameter values can be found in the previous literature.[47,48] According to the previous literature, the intercalation of sodium ions into iron sulfide nanocrystals (Na_xFeS) and hard carbon may lead to a reduction in sodium ion diffusivity, leaving fewer sites available for additional sodium ions to diffuse into.[49,50] However, the phase transition of Na_xFeS to metallic Fe and Na_2S enhances the sodium ion diffusivity, which is ascribed to the low crystallinity of metallic Fe and weaker ionic bonds of Na_2S.[42,51] Considering these factors and the gradual increase in diffusion coefficient values during the sodiation process (Figure 7g–i), it can be seen that the phase transition of Na_xFeS to metallic Fe and Na_2S had a larger effect on the total sodium-ion diffusivity of the electrodes, regardless of the high contents of carbon components in these electrodes. Consequently, the $D_{\mathrm{Na+}}$ values of the three samples gradually decrease as the charging process progresses. It is worth noting that the lowest diffusivity observed in D-FeS-C-CNT can be attributed to the nanocrystals located within the densely structured carbon material. To further investigate the influence of FeS-C nanostructures on resistance and sodium ion diffusivity after cycling, in situ EIS measurements were performed after 100 cycles, as depicted in Figure 7j–r. Comparing the results with the initial cycle, the charge transfer kinetics and sodium ion diffusivity of the three samples improved due to the activation process in the initial few cycles. Furthermore, unlike the R_{tot} variations at the initial discharge (Figure 7d–f), the R_{tot} values after 100 cycles (Figure 7m–o) were gradually increased during the discharge process, which was mainly ascribed to the volume expansion. This suggests that the decrease in R_{tot} values observed during the initial discharge (Figure 7d–f) could be attributed to the formation of ultrafine nanocrystals due to the conversion reaction as well as the initial activation of the hard carbon component.[43,44,52] Interestingly, in contrast to the first cycle, P-FeS@C-CNT exhibited superior charge transfer and sodium ion diffusion kinetics compared to the other two samples. This can be attributed to the small-sized nanocrystals and porous structure of P-FeS@C-CNT, which effectively accommodates the significant volume changes during repeated cycling. On the other hand, D-FeS-C-CNT and D-FeS-C, with their dense structures, are prone to structural damage, resulting in sluggish charge transfer and diffusion kinetics after cycling. The fracturing and pulverization of FeS-C particles, along with the formation of thick SEI layers, likely contribute to this behavior. Interestingly, despite the morphological characteristics mentioned earlier for D-FeS-C-CNT, it exhibited faster charge transfer and sodium ion diffusivity than D-FeS-C after 100 cycles. This indicates that the nanocrystals within the carbon structure effectively mitigate the stress caused by significant volume changes during cycling. The in situ EIS data after 150 cycles also demonstrate the excellent cycling stability of P-FeS@C-CNT, as depicted in Figure S11, Supporting Information. The degradation trend in charge transfer kinetics and sodium ion diffusivity, as influenced by the morphological characteristics of the three samples, exhibits similar behavior as shown in Figure 7j–r. Notably, despite D-FeS-C having the highest average R_{tot} value due to structural instability, the severe pulverization of D-FeS-C helps alleviate the stress resulting from volume expansion during the sodiation process. Consequently, D-FeS-C shows the smallest variation in R_{tot}, as depicted in Figure S11f, Supporting Information.

The electrochemical performance of the three samples as anodes for sodium-ion batteries was evaluated in **Figure 8**. The initial galvanostatic discharge/charge curves of the three samples at a current density of 0.2 A g^{-1} showed good fitting to the redox peaks observed in the CV curves, as depicted in Figure 8a. P-FeS@C-CNT, D-FeS-C-CNT, and D-FeS-C exhibited initial discharge capacities of 1027, 888, and 845 mA h g^{-1}, respectively, with initial coulombic efficiencies (ICE) of 39%, 45%, and 43%, respectively. The presence of a porous structure in P-FeS@C-CNT led to higher reactivity and increased formation of SEI layers, resulting in a relatively lower ICE value. The rate capabilities of the three samples were compared, as shown in Figure 8b. At current densities of 0.2, 0.5, 1, 2, 3, 4, and 5 A g^{-1}, P-FeS@C-CNT exhibited reversible discharge capacities of 407, 345, 284, 210, 162, 126, and 100 mA h g^{-1}, respectively, and the capacity returned to 432 mA h g^{-1} when the current density was reduced back to 0.2 A g^{-1}. The discharge capacities of D-FeS-C-CNT and D-FeS-C at a current density of 5 A g^{-1} showed slightly higher values of 118 and 132 mA h g^{-1}, respectively. Up to a relatively low current density of 1 A g^{-1}, P-FeS@C-CNT exhibited slightly higher rate capabilities. However, at high current densities between 2 and 5 A g^{-1}, it demonstrated relatively lower rate capabilities compared to the other two samples. This suggests that at high current densities, nanocrystals exposed on the surface of the carbon shell contribute more to the rate performance than those located inside porous carbon structures. On the other hand, considering cycle stability, the encapsulated nanocrystals exhibited superior performance compared to the exposed nanocrystals. As depicted in Figure S12, Supporting Information, the subsequent cycle performances of the three samples at a current density of 0.5 A g^{-1} indicate the stable cycling of P-FeS@C-CNT for 200 cycles, while the other two samples exhibited continuous capacity fading after 120 cycles. The in situ EIS data in Figure 7j–r and Figure S11, Supporting Information confirm that the iron sulfide nanocrystals encapsulated in the porous carbon structure are

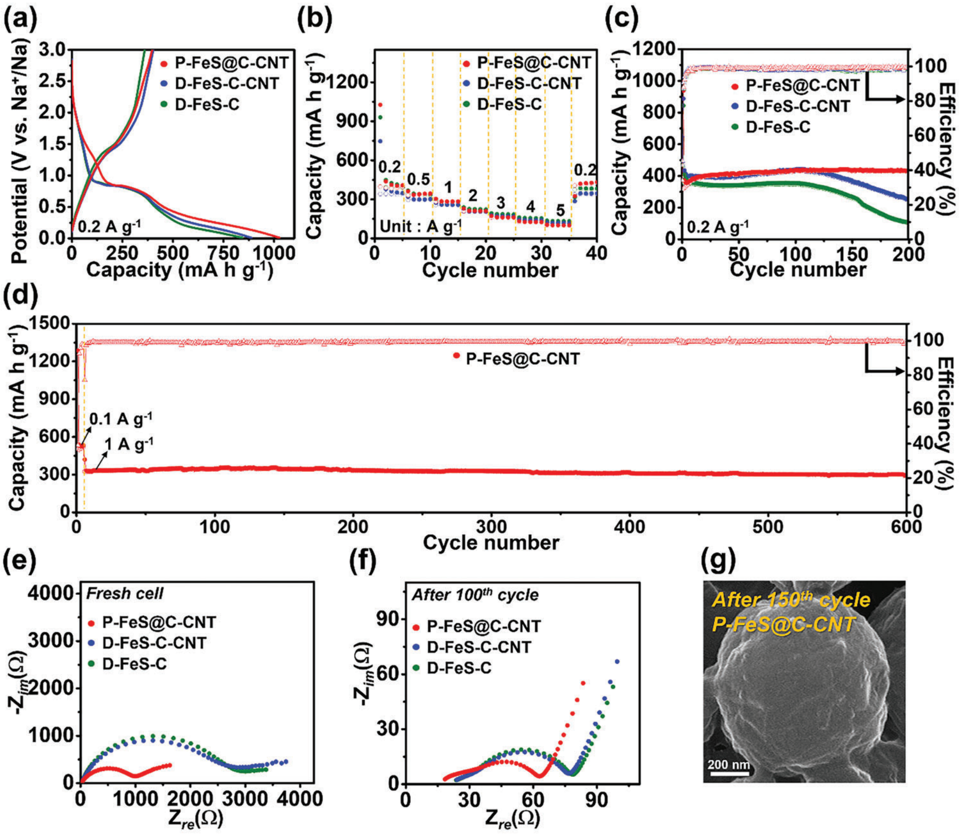

Figure 8. Electrochemical properties of P-FeS@C-CNT, D-FeS-C-CNT, and D-FeS-C electrodes: a) initial discharge/charge curves, b) rate performances, c) cycle performances at a current density of 0.2 A g^{-1}. d) Long term cycling performance of P-FeS@C-CNT at a current density of 1 A g^{-1} with activation firstly at a cycling rate of 0.1 A g^{-1} for five times. Nyquist plots of e) fresh cells and f) after 100 cycles, g) SEM images of P-FeS@C-CNT after 150 cycles.

beneficial in accommodating volume stress during cycling, resulting in excellent cycling stability. Consequently, the cycle performances of the three samples in Figure 8c also demonstrate the superior cycle stability of P-FeS@C-CNT, with a capacity retention of 117% compared to the 2nd cycle. From the 2nd to the 200th cycle, the discharge capacity of P-FeS@C-CNT further increased from 370 to 432 mA h g^{-1} due to increased capacity during the initial 20 cycles. The initial capacity increase of P-FeS@C-CNT is commonly attributed to the formation of a polymeric gel-like film, which corresponds to the reversible formation of SEI layers.[53,54] In contrast, the discharge capacities of D-FeS-C-CNT and D-FeS-C after 200 cycles were 257 and 107 mA h g^{-1}, respectively. To get the actual sodium-ion storage of the carbon component in the P-FeS@C-CNT, the cycle tests of bare P-C-CNT anode for SIBs were conducted as shown in Figure S13, Supporting Information. In this study, the porous carbon components surrounding the CNTs, which were derived from the decomposition of PVP and sucrose under 1000 °C, had characteristics of amorphous carbon and some portions of hard carbon. Therefore, the initial Coulombic efficiency of P-C-CNT showed a very low value (14%), which was attributed to the irreversible absorption of sodium ion to the functional group over P-C-CNT and the formation of solid electrolyte interface (SEI) film within the micropores inside or on the surface of the P-C-CNT. The initial discharge capacity of P-C-CNT was 700 mA h g^{-1} at a current density of 0.2 A g^{-1}, and a gradual decrease in discharge capacity from 140 to 104 mA h g^{-1} was observed between the 2nd and the 200th cycles. Considering carbon contents in the P-FeS@C-CNT, which was proved in the TG data (Figure S10, Supporting Information), the actual capacity contributed by carbon in P-FeS@C-CNT after 200th cycle is calculated to 58 mA h g^{-1}. Furthermore, P-FeS@C-CNT exhibited excellent cycling performance even at a high current density of 1 A g^{-1}, as shown in Figure 8d. In the long-term cycling, P-FeS@C-CNT maintained a reversible discharge capacity of 293 mA h g^{-1} for 600 cycles, showing improved electrochemical performance compared to previously reported iron sulfide-carbon composite anode materials for SIBs (Table S2, Supporting Information). The ex situ EIS measurements conducted before cycling and after 100 cycles also demonstrated the excellent cycle stability of P-FeS@C-CNT. Prior to cycling, the P-FeS@C-CNT electrode exhibited the smallest R_{tot} values among the three electrodes, indicating that the porous carbon structure of P-FeS@C-CNT facilitates fast electrolyte penetration and boosts the aging process of sodium ions. Additionally, the presence of additional semicircles after 100 cycles indicates the formation of SEI layers, with R_{tot} values of 64, 78, and 80 Ω for P-FeS@C-CNT, D-FeS-C-CNT, and D-FeS-C, respectively. The higher R_{tot} values of D-FeS-C-CNT and D-FeS-C can be attributed to the formation of thick SEI layers resulting from the continuous structural destruction during repeated cycling. This observation is further

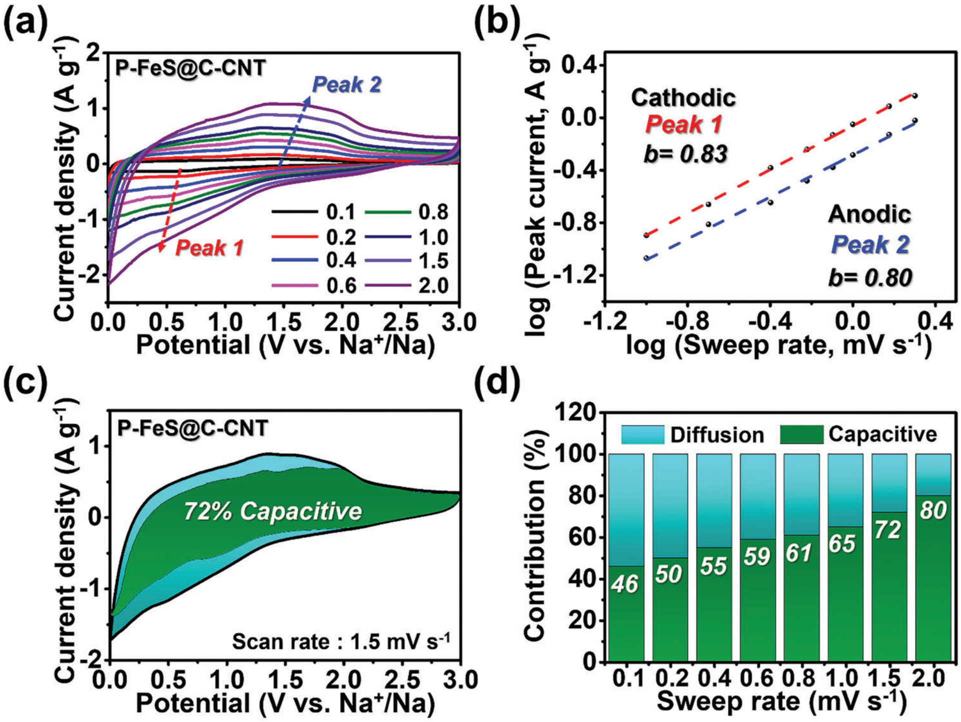

Figure 9. a) CV curves of P-FeS@C-CNT at various scan rates, b) fitted log (peak current) versus log (scan rate) for peaks 1 and 2, c) CV curves of P-FeS@C-CNT showing capacitive contribution (green colored area) to the total current, and d) capacity contribution at different scan rates of P-FeS@C-CNT.

supported by the SEM images of the cycled electrodes, as shown in Figure 8g and Figure S14, Supporting Information. P-FeS@C-CNT electrode exhibits excellent stability even after 150 cycles, while D-FeS-C-CNT and D-FeS-C electrodes exhibit severe structural breaking.

Apart from the stable cycling performance of P-FeS@C-CNT, the low ICE value (39%), attributed to the high carbon content (56 wt.% calculated from TG data), requires improvement for practical application. In this study, the P-FeS@C-CNT was prepared by infiltration of solution dissolved by 4 g of iron nitrate into the 1 g of porous carbon microsphere powders. The carbon content of P-FeS@C-CNT could be determined by the infiltration amount of iron nitrate into porous carbon microspheres (P-C-CNT). Therefore, to reduce the carbon content in the P-FeS@C-CNT, a higher infiltration amount of iron nitrate is required. To investigate the optimal infiltration amount of iron nitrate into P-C-CNT, excess (6 and 8 g) infiltration amount of iron nitrate was applied to 1 g of P-C-CNT. The SEM images in Figure 2a and Figure S15b–e, Supporting Information revealed obvious morphological differences according to infiltration amount of iron nitrate. In case of optimal infiltration amount (4 g) of iron nitrate (Figure 2a), the iron sulfide nanocrystals were completely encapsulated within the P-C-CNT. On the other hand, in case of excess infiltration amount (6 and 8 g) of iron nitrate (Figure S15b–e, Supporting Information), the iron sulfide nanocrystals were simultaneously observed inside and outside the carbon shell. Additionally, it was found that an increased infiltration of iron nitrate led to a greater exposure of iron sulfide nanocrystals to the outside of the carbon shell. When the infiltration amount was exceeded, the iron nitrate was not sufficiently infiltrated into the pore space of P-C-CNT, resulting in the formation of iron sulfide nanocrystals outside the carbon shell. Furthermore, the electrochemical properties of FeS-C-CNT electrodes, which were formed by excess infiltration amount (6 and 8 g) of iron nitrate, were investigated as anode materials for SIBs (Figure S16, Supporting Information). Compared to the P-FeS@C-CNT (Figure 8a), the electrodes, which were formed by excess infiltration amount (6 and 8 g) of iron nitrate, exhibited higher ICE values (49% and 54%, respectively) due to the lower carbon contents. However, this improvement was accompanied by an unstable cyclic performance due to the structural instability of iron sulfide nanocrystals exposed outside the carbon shell. The development of a carbon substrate with controlled pores capable of accommodating a higher amount of infiltrated iron nitrate would facilitate the high ICE. From this perspective, this study has highlighted the potential for adjusting the porosity of carbon materials by controlling the sucrose content in the spray solution. This indicates significant potential for improvement.

To explore the electrochemical kinetics of Na^+ storage in the three electrodes, CV rate tests were conducted at different scan rates ranging from 0.1 to 2.0 mV s^{-1} (**Figure 9**, and Figures S17 and S18, Supporting Information). The relationship between the scan rate (ν) and the measured current (i) can be described by the following equation, as depicted in the CV curves at various scan rates.

$$\log(i) = b\log(\nu) + \log(a) \tag{5}$$

The b values corresponding to the redox peaks in the three electrodes were determined from log (i) versus log (ν) plots, as shown in Figure 9b, and Figures S17b and S18b, Supporting Information. It can be observed that all three electrodes exhibited high b values during both the reduction (peak 1) and oxidation (peak 2) processes, indicating significant capacitive behavior of the iron sulfide nanocrystals.[55–57] This capacitive behavior likely contributes to the excellent rate capabilities observed in Figure 8b. To further understand the contribution of capacitive capacity and diffusion-controlled capacity, the following equation was used for investigation.

$$i\,(V) = k_1\nu + k_2\nu^{1/2} \tag{6}$$

The parameters $k_1\nu$ and $k_2\nu^{1/2}$ represent the surface capacitive and diffusion-controlled behaviors, respectively.[55–57] At a scan rate of 1.5 mV s^{-1}, the percentage of capacitive contribution (indicated by the green area) in P-FeS@C-CNT, D-FeS-C-CNT, and D-FeS-C electrodes was found to be 72%, 70%, and 71%, respectively, as shown in Figure 9d, and Figures S17d and S18d, Supporting Information. These capacitive contributions exhibited a gradual increase with higher scan rates, further indicating the excellent rate capabilities of the three electrodes.

3. Conclusion

In this study, we propose the use of a highly porous carbon-coated CNT microsphere as an exceptional reservoir for sodium-ion batteries. Through a simple infiltration process followed by sulfidation, we successfully prepared a porous microsphere with iron sulfide nanocrystals encapsulated within a porous carbon structure. The use of porous carbon with multiple voids and an optimized sulfidation method ensures complete encapsulation of the iron sulfide nanocrystals. Importantly, the encapsulation of the nanocrystals within the porous carbon structure provides a beneficial solution to accommodate the significant volume changes that occur during cycling. Additionally, the uniform dispersion of CNTs throughout the composite greatly enhances its electrical conductivity. As a result, the porous FeS-C-CNT composite microsphere exhibits robust cycling stability and high rate capabilities when employed as an anode material for sodium-ion batteries. This rational encapsulation strategy offers a promising approach to overcome the challenges associated with volume change and low conductivity in various applications.

4. Experimental Section

The highly porous carbon-coated CNT microspheres were prepared by spray pyrolysis, selenization, and etching processes. During the spray pyrolysis process, droplets were generated using a 1.7-MHz ultrasonic spray generator consisting of six vibrators. The droplets were carried to a quartz reactor with a length of 1200 mm and diameter of 50 mm maintained at 400 °C using air as a carrier gas at a flow rate of 10 L min^{-1}. The spray solution was prepared by dissolving 0.2 M of Sn(II) oxalate, 0.05 M of magnesium nitrate hexahydrate, 8 g L^{-1} of PVP (M_w = 40 000), a certain concentration of sucrose with a PVP/sucrose weight ratio of 1/2, and 1.6 mg ml^{-1} of acid treated multi-wall CNTs (MWCNTs) in 1 L of distilled water. The acid-treated MWCNTs were obtained by oxidizing MWCNTs through treatment with an HNO_3/H_2SO_4 (1:3 v/v) solution at 70 °C, followed by washing with distilled water. As a comparative sample, the porous carbon-coated CNT dense microspheres were prepared by increasing the sucrose concentration in the spray solution under the same conditions. The amount of sucrose added was determined to be a PVP/sucrose weight ratio of 1/8. The sprayed precursor powders were post-treated in a tube furnace at 1000 °C under a 10% H_2/Ar atmosphere for 3 h and etched by HCl/HNO_3 solution to produce porous carbon-coated CNT microspheres. Based on 1 g of porous carbon-coated microsphere powders, 4 g of iron nitrate nonahydrate ($Fe(NO_3)_3{\cdot}9H_2O$, Samchun Chemical Co. Ltd.) was dissolved in a high-purity solution of ethyl alcohol. The solution was infiltrated into the porous carbon-coated CNT microsphere powders. The infiltrated powders were thoroughly blended with sulfur nanopowders, maintaining an 8:1 molar ratio of sulfur to iron. This mixture then underwent a sulfidation process at 155 °C (12 h) and 400 °C (6 h) under a 10% H_2/Ar atmosphere to form FeS-C-CNT composite microspheres. Detailed information pertaining to the characterization and electrochemical measurements of the prepared samples is provided in Supporting Information.

Supporting Information

Supporting Information is available from the Wiley Online Library or from the author.

Acknowledgements

Y.B.K. and H.Y.S. authors contributed equally to this work. This work was supported by the National Research Foundation of Korea (NRF) grant funded by the Korean government (MEST) (NRF-2022R1F1A1070886). This work was supported by the Chungbuk National University BK21 program (2022). This research was supported by a grant from the Korea Institute of Ceramic Engineering and Technology (KICET).

Conflict of Interest

The authors declare no conflict of interest.

Data Availability Statement

Data sharing is not applicable to this article as no new data were created or analyzed in this study.

Keywords

anodes, encapsulation, iron sulfide, nanostructured carbon, sodium-ion batteries

Received: July 6, 2023
Revised: September 11, 2023
Published online:

---

[1] S. H. Yang, S.-K. Park, G. D. Park, J.-H. Lee, Y. C. Kang, *Small* **2020**, *16*, 2002345.
[2] X. Du, C. Zhao, M. Zhou, T. Ma, H. Huang, M. Jaroniec, X. Zhang, S.-Z. Qiao, *Small* **2017**, *13*, 1602592.
[3] J.-S. Park, S. Y. Yang, J.-K. Lee, Y. C. Kang, *J. Mater. Chem. A* **2022**, *10*, 17790.
[4] Y. Fang, S. L. Zhang, Z.-P. Wu, D. Luan, X. W. D. Lou, *Sci. Adv.* **2021**, *7*, abg3626.

[5] Y. Qi, Q.-J. Li, Y. Wu, S.-J. Bao, C. Li, Y. Chen, G. Wang, M. Xu, *Nat. Commun.* **2021**, *12*, 6347.
[6] H. Li, P. Guo, H. Wang, Y. Guo, Y. Wei, F. Cao, L. Li, H. Wang, *Adv. Funct. Mater.* **2023**, *33*, 2210885.
[7] K. V. Kravchyk, L. Piveteau, R. Caputo, M. He, N. P. Stadie, M. I. Bodnarchuk, R. T. Lechner, M. V. Kovalenko, *ACS Nano* **2018**, *12*, 8297.
[8] A. Kumar, P. Choudhary, A. Kumar, P. H. C. Camargo, V. Krishnan, *Small* **2022**, *18*, 2101638.
[9] N. P. Radhika, R. Selvin, R. Kakkar, A. Umar, *Arabian J. Chem.* **2019**, *12*, 4550.
[10] Y. J. Hong, J.-K. Lee, Y. C. Kang, *J. Mater. Chem. A* **2017**, *5*, 988.
[11] S. Chen, X. Huang, B. Sun, J. Zhang, H. Liu, G. Wang, *J. Mater. Chem. A* **2014**, *2*, 16199.
[12] M. H. A. Shiraz, E. Rehl, H. Kazemian, J. Liu, *Nanomaterials* **2021**, 11.
[13] S. Y. Jeong, S.-K. Park, Y. C. Kang, J. S. Cho, *Chem. Eng. J.* **2018**, *351*, 559.
[14] C. Zhu, X. Mu, P. A. Van Aken, Y. Yu, J. Maier, *Angew. Chem.* **2014**, *126*, 2184.
[15] H. Hu, J. Zhang, B. Guan, X. W. D. Lou, *Angew. Chem., Int. Ed.* **2016**, *55*, 9514.
[16] J. Jiang, C. Ma, T. Ma, J. Zhu, J. Liu, G. Yang, Y. Yang, *J. Alloys Compd.* **2019**, *794*, 385.
[17] X. Han, L. Sun, F. Wang, D. Sun, *J. Mater. Chem. A* **2018**, *6*, 18891.
[18] Z. Zhu, S. Wang, J. Du, Q. i. Jin, T. Zhang, F. Cheng, J. Chen, *Nano Lett.* **2014**, *14*, 153.
[19] M. S. Jo, J. S. Lee, S. Y. Jeong, J. K. Kim, Y. C. Kang, D. W. Kang, S. M. Jeong, J. S. Cho, *Small* **2020**, *16*, 2003391.
[20] G. D. Park, J. H. Choi, D. S. Jung, J.-S. Park, Y. C. Kang, *J. Alloys Compd.* **2020**, *821*, 153224.
[21] Y. B. Kim, H. Y. Seo, S.-H. Kim, T. H. a. Kim, J. H. Choi, J. S. Cho, Y. C. Kang, G. D. Park, *Small Methods* **2023**, *7*, 2201370.
[22] Y. Yang, W. Fu, D. C. Lee, C. Bell, M. Drexler, Z. F. Ma, A. Magasinski, G. Yushin, F. M. Alamgir, *Mater. Today Energy* **2020**, *16*, 100410.
[23] X. Liu, X. Li, X. Lu, X. He, N. a. Jiang, Y. u. Huo, C. Xu, D. Lin, *J. Alloys Compd.* **2021**, *854*, 157132.
[24] L. Yu, L. Qin, X. Xu, K. Kim, J. Liu, J. Kang, K. H. Kim, *Chem. Eng. J.* **2022**, *431*, 133463.
[25] G. M. Tomboc, Y. Wang, H. Wang, J. Li, K. Lee, *Energy Storage Mater.* **2021**, *39*, 21.
[26] Q. Liu, S.-J. Zhang, C.-C. Xiang, C.-X. u. Luo, P.-F. Zhang, C.-G. Shi, Y. Zhou, J.-T. Li, L. Huang, S.-G. Sun, *ACS Appl. Mater. Interfaces* **2020**, *12*, 43624.
[27] J. S. Cho, J.-S. Park, Y. C. Kang, *Nano Res.* **2017**, *10*, 897.
[28] Z. Cao, H. Song, B. Cao, J. Ma, X. Chen, J. Zhou, Z. Ma, *J. Power Sources* **2017**, *364*, 208.
[29] Y. Xiao, J.-Y. Hwang, I. Belharouak, Y.-K. Sun, *ACS Energy Lett.* **2017**, *2*, 364.
[30] S. Y. Lee, Y. C. Kang, *Chem. – Eur. J.* **2016**, *22*, 2769.
[31] H. Wang, X. Qiu, W. Wang, L. Jiang, H. Liu, *Front Chem* **2019**, *7*, 855.
[32] Z. Chen, R. Liu, S. Liu, J. Huang, L. Chen, R. Nadimicherla, D. Wu, R. Fu, *Chem. Commun.* **2020**, *56*, 12921.
[33] J. Liang, S. i. Chen, Z. Fan, S. Zheng, Z. Wang, *Ionics* **2021**, *27*, 4185.
[34] C. Wang, B. Zhang, H. Xia, L. Cao, B. i. Luo, X. Fan, J. Zhang, X. Ou, *Small* **2020**, *16*, 1905853.
[35] G. D. Park, Y. C. Kang, *ACS Sustainable Chem. Eng.* **2020**, *8*, 17707.
[36] Y. Luan, R. Hu, Y. Fang, K. Zhu, K. Cheng, J. Yan, K. Ye. Ye, G. Wang, D. Cao, *Nano–Micro Lett.* **2019**, *11*, 30.
[37] Y. Tan, K. -W. Wong, Z. Zhang, K. M. Ng, *Nanoscale* **2017**, *9*, 19408.
[38] M. Wang, Y. Yang, Z. Yang, L. Gu, Q. Chen, Y. Yu, *Adv. Sci.* **2017**, *4*, 1600468.
[39] D. Yang, D. Yadav, I. Jeon, J. Seo, S. -Y. Jeong, C. R. Cho, *ACS Appl. Mater. Interfaces* **2022**, *14*, 44303.
[40] Y.-X. Wang, J. Yang, S.-L. Chou, H. K. Liu, W.-X. Zhang, D. Zhao, S. X. Dou, *Nat. Commun.* **2015**, *6*, 8689.
[41] G. D. Park, J.-S. Park, J. K. Kim, Y. C. Kang, *Chem. Eng. J.* **2022**, *428*, 131051.
[42] J. Zhang, J. Lin, Y. Zeng, Y. Zhang, H. Guo, *ACS Appl. Energy Mater.* **2019**, *2*, 8345.
[43] S. H. Yang, Y. J. Lee, H. Kang, S.-K. Park, Y. C. Kang, *Nano–Micro Lett.* **2022**, *14*, 17.
[44] S. H. Yang, S.-K. Park, Y. C. Kang, *Nano-Micro Lett.* **2021**, *13*, 9.
[45] M. K. Singh, J. Pati, D. Seth, J. Prasad, M. Agarwal, M. A. Haider, J.-K. Chang, R. S. Dhaka, *Chem. Eng. J.* **2023**, *454*, 140140.
[46] J.-S. Park, S. Yang, Y. C. Kang, *Chem. Eng. J.* **2020**, *393*, 124606.
[47] Z. Wang, K. Dong, D. Wang, S. Luo, X. Liu, Y. Liu, Q. Wang, Y. Zhang, A. Hao, C. He, C. Shi, N. Zhao, *Chem. Eng. J.* **2020**, *384*, 123327.
[48] J. Zheng, P. Yan, W. H. Kan, C. Wang, A. Manthiram, *J. Electrochem. Soc.* **2016**, *163*, A584.
[49] J. Wang, L. Wang, C. Eng, J. Wang, *Adv. Energy Mater.* **2017**, *7*, 1602706.
[50] L. Tao, Y. Yang, H. Wang, Y. Zheng, H. Hao, W. Song, J. Shi, M. Huang, D. Mitlin, *Energy Storage Mater.* **2020**, *27*, 212.
[51] P. Ge, H. Hou, S. Li, L. i. Yang, X. Ji, *Adv. Funct. Mater.* **2018**, *28*, 1801765.
[52] F. Chen, Y. Di, Q. Su, D. Xu, Y. Zhang, S. Zhou, S. Liang, X. Cao, A. Pan, *Carbon Energy* **2023**, *5*, 191.
[53] Q. He, K. Rui, J. Yang, Z. Wen, *ACS Appl. Mater. Interfaces* **2018**, *10*, 29476.
[54] J. Bai, X. Li, G. Liu, Y. Qian, S. Xiong, *Adv. Funct. Mater.* **2014**, *24*, 3012.
[55] C. Cui, Z. Wei, G. Zhou, W. Wei, J. Ma, L. Chen, C. Li, *J. Mater. Chem. A* **2018**, *6*, 7088.
[56] P. Ge, H. Hou, S. Li, L. Huang, X. Ji, *ACS Appl. Mater. Interfaces* **2018**, *10*, 14716.
[57] G. D. Park, S. J. Yang, J.-H. Lee, Y. C. Kang, *Small* **2019**, *15*, 1905289.